Ligand Radicals as Modular Organic Electron Spin Qubits

Jake McGuire,[†] *Haralampos N. Miras,*[†] *James P. Donahue,*[‡] *Emma Richards,*[§] *and Stephen Sproules*[†,*]

[†]WestCHEM, School of Chemistry, University of Glasgow, Glasgow G12 8QQ, United Kingdom

[‡]Department of Chemistry, Tulane University, 6400 Freret Street, New Orleans, Louisiana 70118, United States

[§]School of Chemistry, Cardiff University, Main Building, Park Place, Cardiff CF10 3AT, United Kingdom

Email: stephen.sproules@glasgow.ac.uk

Abstract: The intrinsic redox activity of the dithiolene ligand is presented here as the novel spin host in the design of prototype molecular electron spin qubit where the traditional roles of the metal and ligand components in coordination complexes are inverted. A series of paramagnetic bis(dithiolene) complexes with group 10 metals – nickel, palladium, platinum – provides a backdrop to investigate the spin dynamics of the organic ligand radical using pulsed EPR spectroscopy. The temperature dependence of the phase memory time (T_M) is shown to be dependent on the identity of the diamagnetic metal ion with the short times recorded for platinum a consequence of a diminishing spin-lattice (T_1) relaxation time driven by spin-orbit coupling. The utility of the radical ligand spin center is confirmed when it delivers one of the longest phase memory times ever recorded for a molecular two-qubit prototype.

Introduction

The seminal work of Leuenberger and Loss[1] who proposed encoding quantum information using the spin states of molecular magnets has spurred a frisson of activity in the development of molecule-based electron spin qubits.[2] The advantage of electrons resides in the ease of their initialization and a large gyromagnetic ratio that facilitates their manipulation to effect quantum algorithms.[3,4] The drawback is they tend to have less favorable coherence lifetimes than their nuclear spin counterparts as expressed in terms of the spin-lattice relaxation (T_1) and the phase memory (T_M) times, where the latter represents the lifetime of the superposition state.[5] For spin qubits based on transition metal complexes, this handicap has been conquered by skillful tailoring of the chemical environment about the paramagnetic metal ion to remove components with deleterious effects on the performance. Tactics such as nuclear spin bath control and careful isolation of the paramagnetic center have catapulted the phase memory time of a coordination complex to an astonishing 0.7 ms.[6] When this chemical strategy is used in tandem with pulse optimization,[7] a record T_M = 1.4 ms has been reached, where the single qubit figure of merit matches the best among related matter spin qubits.[8] These long coherence times lead to low error rates and high fidelities that are required for large-scale, fault-tolerant quantum computing.[9]

With the long phase memory times realized, considerable energy is now focused on dissecting the intricacies of spin dynamics essential to quantum information processing and related disciplines.[10-12] While these single-spin qubits are primed for such an undertaking, they do not lend themselves to meeting the equally important challenge of quantum gating and addressability that are requirements for universal quantum computation. To tackle this goal, a new design is needed to produce molecules with more than one spin center that can be selectively controlled to generate entanglement. There have been a few molecular two-qubit systems developed targeting this objective,[13,14] including prototypes that effect universal quantum logic.[15,16] We propose a novel architecture of molecular spin qubits based on paramagnetic coordination complexes where the traditional role of the organic and inorganic components is inverted with spins residing on radical ligands and linked by diamagnetic metal ions. The construct utilizes the ubiquitous dithiolene ligand, which is readily oxidized to create the $S = {}^{1}/_{2}$ center confined to its constituent, nuclear-spin-free $\{S_2C_2\}$ core.[17,18] The spin dynamics of the ligand radical spin host is investigated by pulsed EPR measurements on the homoleptic series $[PPh_4][M(adt)_2]$ (M = Ni (**1**), Pd (**2**), Pt (**3**); adt^{2-} = bis(*p*-anisyl)-1,2-ethenedithiolate). We demonstrate the modular nature of our synthetic approach by electrochemically oxidizing the two metallodithiolene units in $[\{Ni(adt)\}_2(\mu\text{-tpbz})]$ (**4**; tbpz = 1,2,4,5-tetrakis(diphenylphosphino)-benzene). The phase memory time of 3.39(4) μs at 20 K is one of the longest yet reported for a molecular bipartite system.

Results and Discussion

Synthesis and characterization

Compounds **1** – **3** were synthesized in high yield via one-electron reduction of the parent neutral complexes using PPh_4BH_4. The integrity of the sample was conveniently tracked with electronic spectroscopy, as the prominent band is distinct both in energy and intensity when comparing the monoanionic and neutral members that constituent each electron transfer series (Figure S1). The characteristic absorption band is diagnostic of the electronic structure of these bis(dithiolene) species where the low-energy yet high intensity is defined as an intervalence charge transfer (IVCT) transition

to the highest occupied molecular orbital (HOMO), which is the singly-occupied (SOMO) b_{2g} MO in D_{2h} symmetry, from the b_{1u} HOMO-1, which are both ligand-based.[19]

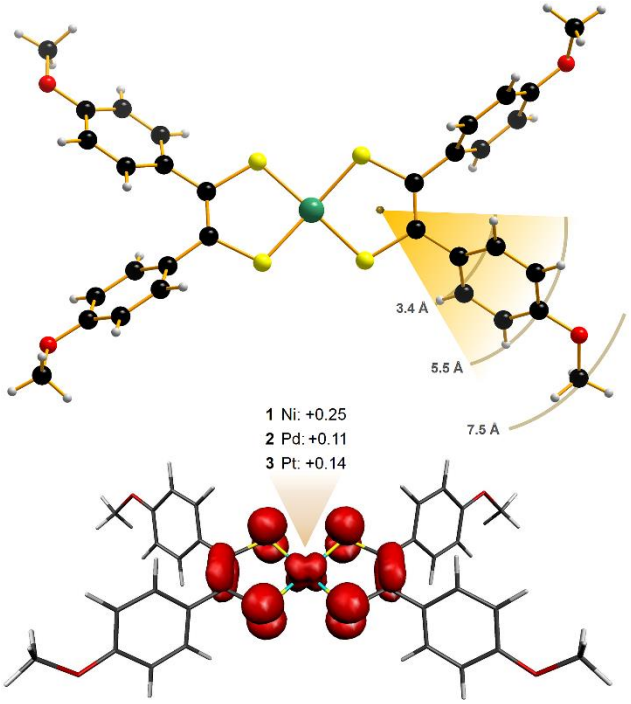

Figure 1. The molecular structure of $[Ni(adt)_2]^{1-}$, showing distance of ligand protons from the spin barycenter (top), and the Mulliken spin density population from ZORA-PBE0 DFT calculations (bottom). The spin density at the metal ion in **1** – **3** is listed. Spin density is plotted with an isovalue 0.004 au.

The molecular structures of **1** – **3** have been characterized by X-ray diffractometry; a representative structure is shown in Figure 1. The central metal ion adopts a square planar geometry with the $\{NiS_4\}$ unit in **1** exhibiting the largest drift toward tetrahedral ($\alpha = 17.6°$). This is a consequence of crystal packing as evidenced by the perfectly planar geometry ($\alpha = 0°$) of the complex ion with a $[NEt_4]^+$ counterion.[20] The anisyl substituents are rotated relative to the $\{S_2C_2\}$ plane at angles ranging 42 – 86° across the series. Therefore via induction, the anisyl group is electron donating reflecting the softer, more polarizable sulfur atoms compared with aromatic dithiolenes or maleonitrile dithiolate, mnt.[21] An important consideration for the forgoing examination of the spin dynamics of this molecular building block is the presence of protons on the periphery of the ligand. Despite the

absence of conjugation that confines the spin density to the $\{S_2C_2\}$ core (Figure 1), the vocal nuclear spin of protons presents an efficient decoherence pathway through dipolar coupling.[10,22] The three types of proton in the ligand – two aromatic and one methyl – are on average 3.4 Å, 5.5 Å and 7.5 Å, respectively, away from the spin barycenter (Figure 1). The orbital parentage manifests in the intraligand bond distances for **1** – **3**. The average S–C bond distance of ca. 1.74 Å and average C–C distance of ca. 1.37 Å are shorter and longer, respectively, than the corresponding bond lengths in the dianionic dithiolate form of the ligand (Table S2). This is characteristic of an oxidized dithiolene, which due to the centrosymmetry of each complex, is distributed over both ligands. The electronic structure of **1** – **3** is defined as $[M^{II}(L_2^{3-\bullet})]^{1-}$ (L = dithiolene), which is an abridged description derived from the limiting resonance forms $[M^{II}(L^{2-})(L^{-\bullet})]^{1-} \leftrightarrow [M^{II}(L^{-\bullet})(L^{2-})]^{1-}$.[19]

Continuous-wave EPR spectroscopy

The cw X-band EPR spectra of **1** – **3** recorded in frozen CH_2Cl_2/DMF solution at 130 K display signals typical of an $S = {}^1/_2$ system with rhombic *g*-values in agreement with those reported in the literature.[23] The profiles for all three spectra are similar with $g_1 > g_2 > g_e > g_3$ (Table 1). The spectrum of **2** exhibits weak shoulders about each *g*-value indicating the presence of hyperfine splitting from ^{105}Pd ($I = {}^5/_2$, 22.2% abundant), which are most pronounced on the low-field lines (Figure S7). Spectral simulation was achieved with $A = (9.0, 5.9, 4.6) \times 10^{-4}$ cm^{-1}. A more prominent hyperfine interaction is observed in the spectrum of **3**, where coupling to the ^{195}Pt ($I = {}^1/_2$, 33.8% abundant) isotope yielded $A = (-33, -106, -83) \times 10^{-4}$ cm^{-1} (Figure S9). The larger coupling in **3** is a direct consequence of the nuclear *g*-value of ^{195}Pt ($g_N = 1.219$) which is roughly 5 times larger than that of ^{105}Pd ($g_N = -0.256$). The more meaningful measure of metal content in the magnetic orbital is the rhombicity of the *g*-values which ranges from 0.10 for **2** to 0.66 for **1** (Table 1). The low rhombicity as well as the low isotropic part of the magnetic hyperfine coupling, indicates that the metal contribution to the SOMO is smallest for **2**. Conversely, **1** being the most rhombic has the largest metal contribution to its magnetic orbital. The anisotropy of the *g*-values stems from the spin-orbit coupling (SOC) constant of the metal center tempered by its contribution to the ground state. As SOC commutes as Z^4,[24] the largest *g*-anisotropy is observed for **3** because of the greater SOC

constant of platinum (Z = 78). The equivalent *g*-anisotropy for **1** and **2** reflects the smaller palladium content to the SOMO in the latter despite having the larger SOC constant. Interestingly, the metal content as assessed by *g*-anisotropy is also modulated by the dithiolene ligand, being larger for aromatic-type dithiolenes such that a more significant proportion of the spin resides on the alkyl dithiolene variant used here.[21,25]

Computations

The geometry-optimized structures for the complex anions in **1** – **3** are in excellent agreement with the experimental data, with the metal-sulfur and intraligand bond distances and angles accurately reproduced (Table S2). Moreover the optimized structures are strictly planar demonstrating the modest tetrahedralization about the nickel ion in **1** is a consequence of crystal packing. Inspection of the frontier MOs reveals four metal d orbitals lower in energy than the ligand-based b_{2g} and b_{3g} (D_{2h} point group) which undergo symmetry-allowed π interactions with metal d orbitals.[19] The b_{2g} symmetric SOMO is ligand-centered such that the electronic structure is best represented as $[M^{II}(L_2^{3-\bullet})]^{1-}$. The unpaired spin is delocalized across both ligands as regulated by the metal ion, whose contribution trends Ni > Pt > Pd across the series (Table 1). As a consequence **2** has a low spin density of 0.11 at the Pd(II) ion indicating an almost negligible contribution from the Pd(III) configuration to the ground state. In contrast, the 0.25 spin density at nickel shows enhanced Ni(III) character in **1** that accounts for its EPR spectral profile. The electronic structure has been verified by very accurate calculation of the *g*-values for **1** – **3** (Table 1). This level of precision allows for meaningful insight that correlates composition and electronic structure factors on the spin dynamics of molecular qubits based on coordination complexes.

Table 1. Summary of Experimental and Calculated Data[a] for **1** – **3**

	1	**2**	**3**	
M	Ni	Pd	Pt	
ζ_{nd} / cm^{-1} [b]	700	1300	3400	
%M [a]	25.2	12.8	18.9	
ρ_M [a]	0.25	0.11	0.14	
g_1	2.1182 (2.0979)	2.0508 (2.0521)	2.1653 (2.1864)	
g_2	2.0402 (2.0650)	2.0419 (2.0487)	2.0654 (2.1062)	
g_3	1.9993 (2.0013)	1.9628 (1.9671)	1.8472 (1.8644)	
R_g [c]	0.66	0.10	0.31	
Δg [d]	0.1189	0.0880	0.3181	
B_0 / mT	340.6	343.3	339.1	344.5[e]
$T_{1,s}$ / ms [f]	6.31(3)	4.99(1)	1.64(2)	1.72(2)
$T_{M,s}$ / µs [f]	4.89(1)	2.07(2)	3.63(2)	3.64(2)
Ω_R / MHz [g]	13.6	15.5	14.5	

[a] From ZORA-PBE0 level of theory (calculated *g*-values in parenthesis). [b] Values taken from ref. [26]. [c] Rhombicity, $R_g = (g_1 - g_2)/(g_1 - g_3)$. [d] *g*-anisotropy, $\Delta g = g_1 - g_3$. [e] B_0 = 344.5 mT corresponding to the high field hyperfine line of g_2 (see Figure S16). [f] Relaxation time at 10 K (error given in parenthesis). [g] Rabi frequency from nutation experiment at 10 K and 6 dB microwave attenuation.

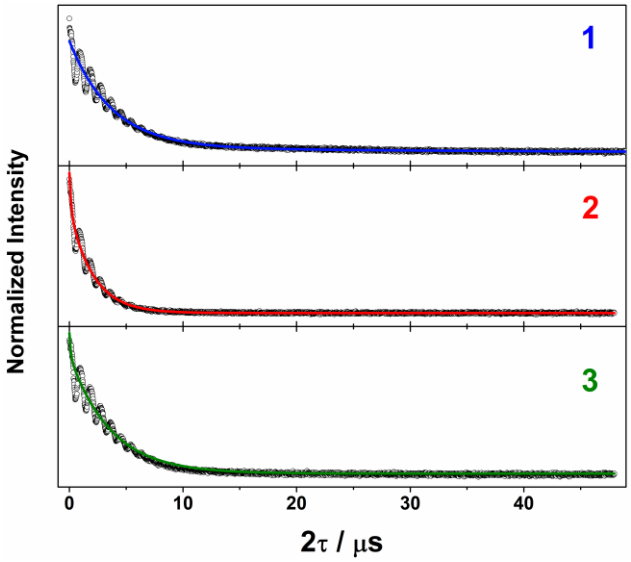

Figure 2. Comparison of the Hahn echo data (open circles) and corresponding biexponential fit (solid lines) for **1** – **3** recorded in 2% CD_2Cl_2/DMF-d_7 at 10 K. Fit parameters are given in Tables S6–S8.

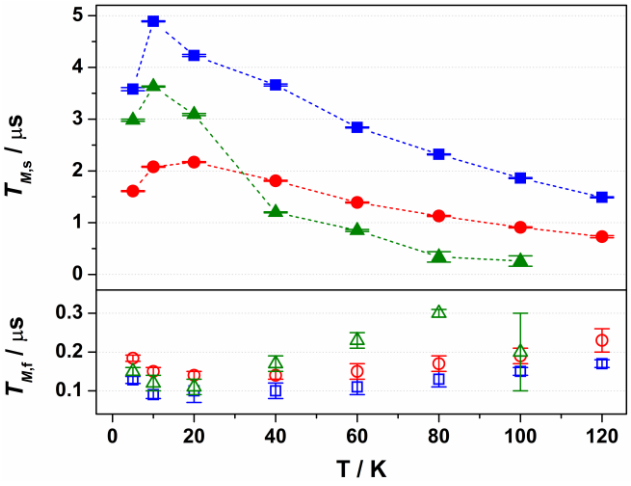

Figure 3. Comparison of the slow (top) and fast (bottom) contributions to phase memory time (T_M) for **1** (squares), **2** (circles) and **3** (triangles) over the temperature range 5 – 120 K. Error bars are based on the standard deviation of the fit (Tables S6–S8).

Pulsed EPR spectroscopy

The decoherence of the spin superposition as quantified by the phase memory time was investigated for **1** – **3** over the temperature range 5 – 120 K on 1 mM solutions in 2% CD_2Cl_2/DMF-d_7. The decay of the Hahn echo measured at the magnetic field corresponding to the absorption maxima (g_2) in the

EPR spectrum follows a biexponential profile; the Hahn echo decay for **1 – 3** measured at 10 K are compared in Figure 2. The biexponential fit gives an estimate for the fast ($T_{M,f}$) and slow ($T_{M,s}$) relaxation processes, with the latter used as the qubit's decoherence parameter. The slow component is longest for **1** at 4.89(1) μs, and shortest for **2** at 2.07(2) μs, with **3** residing between these times at 3.63(2) μs (Figure 3). These times are equal to or eclipse a swathe of $S = {}^1/_2$ coordination complexes reported recently;[2] the few with phase memory times that surpass this have their composition and environment purged of nuclear spins.[6,11,25] The phase memory time displays no orientation dependence nor does it correlate with *g*-anisotropy as observed previously.[25,27] The variation within the series of **1** > **3** > **2** is directly correlated to the spin density at the metal center (vide supra). The major contributor to spin decoherence is electron-nuclear spin interaction, which is the dominant factor at very low temperatures (<30 K). The nuclear spin bath comprises protons on the anisyl substituents of the dithiolene ligand, the protons and phosphorus atom (^{31}P $I = {}^1/_2$, 100% abundant) of the PPh_4^+ counterion, and the ^{2}H nuclei present in the solvent glass. The electronic structure of **1** – **3** differ in the degree of spin density distributed on the $\{S_2C_2\}$ unit of the dithiolene as opposed to the superexchange center that is the metal ion. The pitch of the proton laden anisyl substituents to a non-conjugated orientation with the dithiolene core ensures ^{1}H interaction is dipolar and governed by the interspin distance. Here with the locus of the spin on the ligand, only the methoxy groups lie beyond the spin-diffusion barrier (Figure 1).[10,22] As this distance is identical across the series, interactions from the ligand protons are essentially the same for all complexes. Likewise the metal hyperfine interaction observed in the cw spectra for **2** and **3** has negligible impact on $T_{M,s}$, as ^{195}Pt has the largest coupling but not the shortest decoherence time. Shifting to the high-field hyperfine component about g_2 (B_0 = 344.5 mT) couples the electron and nuclear spin transition allowing access to quantum coherences within a manageable field range to build up a multi-qubit ensemble within single molecule.[28] Therefore it is noteworthy that simultaneous hyperfine transition does not appreciably alter $T_{M,s}$ for the electron spin (Table 1; Figure S20). The distribution of spin density away from the metal ion and the disposition of the SOMO orthogonal to the plane of the complex facilitates greater interaction with the solvent medium. This can be described as an electrostatic interaction between

deuterons and the electronegative $\{S_2C_2\}$ core of the spin host, as evidenced by the modulation in the Hahn echo decay (Figure 2).

There is an overall increase in the relaxation rate with increasing temperature; however, the temperature dependence is markedly different for **3** compared to **1** and **2** (Figure 3). Although all exhibit a shorter $T_{M,s}$ at 5 K than 10 K indicating possible precipitation of some of the complex that create grain boundaries within the frozen glass, which is not uncommon for these molecular systems.[6,8,10,29] In contrast to **1** and **2**, **3** shows a dramatic decrease in $T_{M,s}$ above 20 K. Molecular motion, principally methyl group rotation is touted as the source of decoherence above 40 K where the frequency aligns with the experimental timescale, however this will be uniform across this series. Rather, the shortening of $T_{M,s}$ of **3** is driven by a comparable reduction in the spin-lattice relaxation time which is the ultimate limit for $T_{M,s}$.[30] This striking decrease in spin-lattice relaxation leads to $T_{M,f}$ and $T_{M,s}$ approaching parity and prevents measurement of the Hahn echo decay above 100 K (Figure 3).

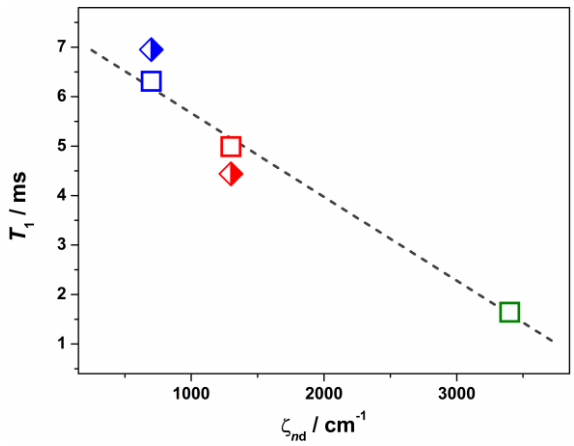

Figure 4. Linear correlation of the experimental spin-lattice relaxation time for **1** (blue), **2** (red) and **3** (green) on the spin-orbit coupling constant (ζ) for the metal ion. Diamonds represent the calculated $T_{1,s}$ for **1** (blue) and **2** (red) relative to **3**.

Spin-lattice relaxation times for **1** – **3** have been obtained from a three-pulse inversion recovery experiment. A biexponential fit applied to the data yielded fast ($T_{1,f}$) and slow ($T_{1,s}$) relaxation processes, where the former is attributed to spectral diffusion and the latter assigned as the spin-lattice

relaxation time. Overall the $T_{1,s}$ times at 10 K are 2–3 orders of magnitude longer than the phase memory time (Table 1). The difference in $T_{1,s}$ across the series represents the most unambiguous demonstration of the intrinsic electronic properties of the atomic constituents of the qubit on its performance. Specifically, the $T_{1,s}$ time is directly correlated to the SOC constant of the metal ion as group 10 is descended (Figure 4). This is the same trend observed in the *g*-anisotropy of the cw EPR spectra and the intensity of the signature electronic transition in these complexes (Figure S1). The significance of SOC has been previously shown to impact spin-lattice times when comparing first- and second-row metals in systems where the metal is the spin host.[27,31] Here, with an unpaired electron predominantly on the ligand, the metal ion presents a heavy-atom effect – a phenomenon that has been exploited in a range of materials, most notably enhancing the performance of semiconductors in spintronic devices.[32] At the measurement temperature, a direct spin relaxation process is dominant,[33] but as the temperature increases the Raman mechanism takes precedence[34] and becomes more efficient with increasing SOC.[35] While relaxation times cannot be directly computed, we have used the calculated electronic structure parameters to estimate $T_{1,s}$ for **1** and **2** when compared to that for **3**. This estimate uses the ratio of the SOC constant for Ni and Pd to Pt, and the parentage of the spin in the molecule that resides on the metal ion (Table 1). These estimates are compared to the experimental values in Figure 4, and the good agreement obtained highlights the intrinsic association between SOC and spin-lattice relaxation such that it is an important consideration in the makeup of any spintronic system. We have begun to explore using these molecules as an alternative to metal dichalcogenides in graphene-based heterostructures.[36]

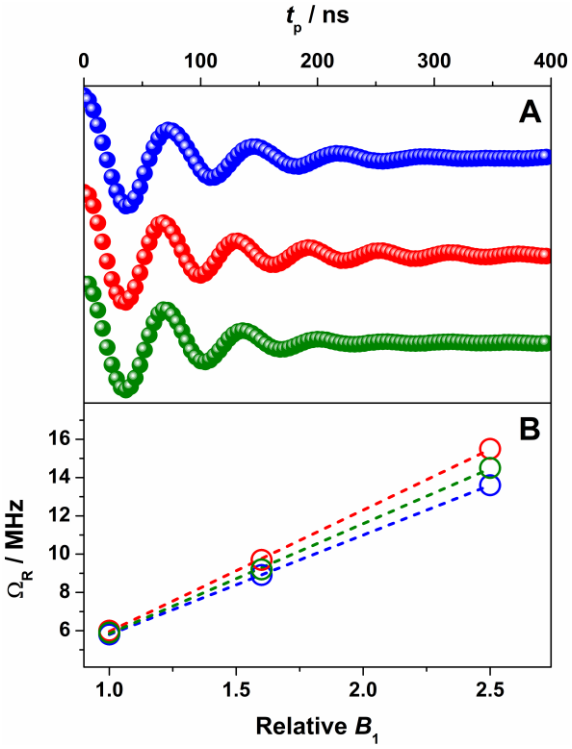

Figure 5. (a) Comparison of the Rabi oscillations for **1** (blue, top), **2** (red, middle) and **3** (green, bottom) at 10 K and 6 dB microwave attenuation. (b) Linear dependence of the oscillation frequency (Ω_R) with respect to the B_1 field. Dashed traces represent line of best fit for **1** – **3**.

To demonstrate coherent spin control, echo-detected nutation experiments were performed by applying a microwave pulse of duration t_p to produce Rabi-like oscillations between two states that correspond to arbitrary superpositions of the electron spin (Figure 5a). Confirmation that these are Rabi oscillations comes from the linear dependence of the oscillation frequency (Ω_R) with the applied microwave amplitude (B_1), which was varied by selecting microwave attenuations of 6, 10 and 14 dB (Figure 5b). Changes in the oscillations were observed at t_p > 400 ns which were independent of the microwave attenuation and arise from the electron spin interacting with surrounding protons.[37]

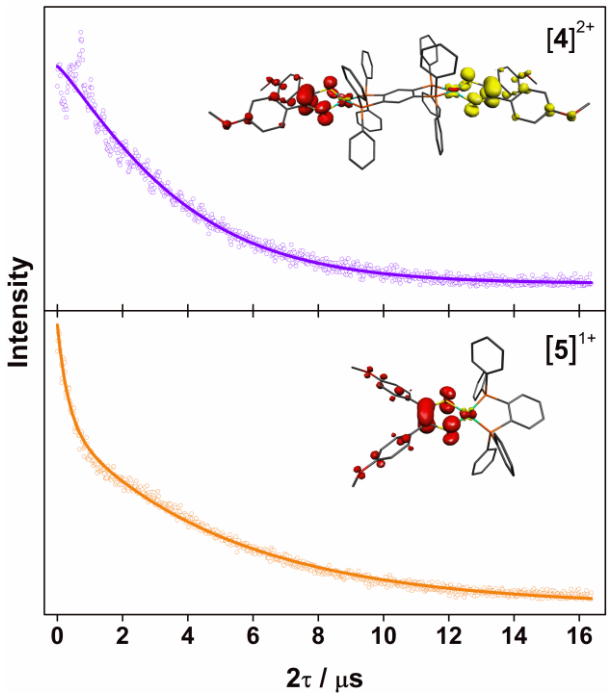

Figure 6. Hahn-echo decay (open circles) and biexponential fit (solid line) of an electrochemically-generated 1 mM solution of $[\mathbf{4}]^{2+}$ and $[\mathbf{5}]^{1+}$ in CH_2Cl_2 solution (0.10 M $[N(^nBu)_4]PF_6$ supporting electrolyte) at 20 K. Insets show domain of the unpaired electrons from a Mulliken spin density analysis (red: α-spin; yellow: β-spin).

To expand the utility of the radical ligand as spin host, we have developed a series of heteroleptic metallodithiolene complexes as platform for implementing two-qubit quantum gates.[17,18,38] The central design strategy involves $\{MS_2P_2\}$ building blocks where the metal is coordinated by a redox-active dithiolene ligand on one side and a redox-inert diphosphine ligand on the other. The latter serves as the vector of propagation, and we have synthesized complexes with two metallodithiolene units linked via a tetraphosphine bridge,[17,18] which can be further elaborated into what can be considered multi-qubit polymers.[39] The synthesis is highly modular, where metals and ligands are selectively installed and positioned in a way that infuses the system with an unprecedented degree of control that fosters single qubit addressability. We can demonstrate this potential with the compound $[\{Ni(adt)\}_2(\mu\text{-tpbz})]$ (**4**). Essentially this is an expanded bis(dithiolene) complex, where the metal ions in the monometallic complexes **1** – **3** are now replaced by the {M(μ-tpbz)M} spacer that separates the terminal dithiolene ligands by ca. 1 nm.[17] Charge-neutral **4** is readily oxidized at very mild potential;

the two-electron event produces the diradical [**4**]$^{2+}$ where each dithiolene now possess an unpaired spin giving a near degenerate singlet-triplet ground state. The optimized structure exhibits the same intraligand bond distances consistent with a coordinated dithienyl radical (Figure S32). Aside from the inherent air stability of this diradical, it is the first cationic molecular spin qubit whose electrostatic field perturbs the interaction with decohering hydrogen atoms in the solvent shell compared with its anionic counterparts.[2] The importance of electrostatics and charge distribution on spin relaxation lifetimes has recently been investigated by Freedman and co-workers.[22] The cw EPR spectrum is characterized with miniscule anisotropy (g = 2.010, 2.017, 2.007) and a vanishingly small zero-field splitting of the S = 1 state of D = -0.0018 cm^{-1} and negligible rhombicity (Figure S25).[17] From the fluid solution spectrum gives a partially resolved hyperfine structure that shows equivalent coupling from all four ^{31}P nuclei coupling revealing $J >> h\nu$.[40] such that the estimate provided by DFT calculations of -3.1 cm^{-1} is very reasonable, and underscores the near degenerate singlet-triplet ground state in [**4**]$^{2+}$ (Figure S34). The effect of the intramolecular spin coupling (J and D) on the phase memory time of this dicationic complex has been measured at 20 K on a 1 mM sample of the complex electrochemically generated in CH_2Cl_2 solution containing 0.1 M [N(^{n}Bu$_4$)]PF$_6$ as electrolyte, i.e. a fully protiated environment. The result is compared to the corresponding monospin species, [Ni(adt)(dppb)]$^{1+}$, [**5**]$^{1+}$, which represents the bipartite system sans intramolecular spin coupling (Figure 6). A biexponential fit to the Hahn echo decay yielded $T_{M,s}$ of 3.39(4) μs for [**4**]$^{2+}$ S = 1 and 5.16(6) μs for [**5**]$^{1+}$ S = $^1/_2$ at 20 K, where the impact of intramolecular spin coupling in the former results in ca. 30% reduction of the phase memory time. The longer time for [**5**]$^{1+}$ compared with **1** is consequence of the miniscule spin density (6%) on the nickel ion (Figure 6 inset).

Conclusion

This work represents the first study that utilizes the organic component of coordination complexes – the ligand – as the spin host in a molecular spin qubit. The redox-active dithiolene ligand bearing a nuclear-spin-free core affords long phase memory times approaching 5 μs that are equal to or exceed those reported for related S = $^1/_2$ complexes typically with V(IV) and Cu(II) paramagnetic ions.[2] The

temperature dependence of the phase memory time is limited by spin-lattice relaxation, which is dramatically shortened when descending group 10 where there is a concomitant increase in the SOC constant for the metal ion. The efficacy of the dithiolene radical as a spin host was extended to heteroleptic complexes, which present a convenient synthetic route to preparing multi-qubit ensembles. The long phase memory time for the prototype two-qubit complex [**4**]$^{2+}$ surpasses lifetimes recorded for all other transition-metal-based two-qubit species at an equivalent temperature.[13,15,41] Moreover this molecular system delivers sufficiently long relaxation times negating any need to optimize the surrounding environment. Key to the challenge of single qubit addressability, we demonstrate electrochemical activation of the spin qubit which is an effective handle to switch the qubit "on" and "off" by applying an appropriate potential, which occurs on a timescale orders of magnitude faster than the lifetime of the superposition state.[3,42] The ability to electrically activate individual qubits is achieved by altering the metal and ligand components of the molecule, and therein lies the ability to switch between various spin states and entanglement scenarios. We will continue to develop this platform with the aim of executing electrically operated multi-qubit quantum gates.

Experimental Section

Synthesis. The compounds [M(adt)$_2$] (M = Ni, Pd, Pt) were prepared following the procedure of Schrauzer and Mayweg.[43] [PPh$_4$][BH$_4$] was synthesized following the literature method.[44]. Solvents either were dried with a system of drying columns from the Glass Contour Company (CH_2Cl_2, hexanes) or freshly distilled according to standard procedures (CH_3OH).[45] Dichloromethane-d_2 and *N*,*N*-dimethylformamide-d_7 were degassed by six successive freeze pump thaw cycles and dried over 3 Å molecular sieves prior to use.

[PPh$_4$][M(adt)$_2$] {M = Ni (1), Pd (2), Pt (3)}. A 50 mL Schlenk flask containing [M(adt)$_2$] (0.1 mmol) dissolved in CH_2Cl_2 (10 mL) was treated with [PPh$_4$][BH$_4$] (0.1 mmol) and stirred for 30 min at ambient temperature. The solvent was removed under reduced pressure, and the residue was

recrystallized from CH_2Cl_2/CH_3OH to give a microcrystalline product. Yield: 84% (**1**), 89% (**2**), 87% (**3**). ESI mass spectrometry confirmed the complex ion $[M]^-$ in the negative ion mode which was accompanied with the singular presence of PPh_4^+ in the positive ion mode. Conversion of the neutral to the monoanionic species was further confirmed by recording the electronic spectra of **1** – **3** which are distinct from their charge-neutral precursors (Figure S1).

X-ray Crystallographic Data Collection and Structure Refinement. Diffraction quality crystals of **1** – **3** were obtained by slow diffusion of hexanes into a concentrated dichloromethane solution of the complex. The crystals were coated with paratone oil and mounted on the end of a nylon loop attached to the end of the goniometer. Data were collected with a Bruker SMART APEX CCD diffractometer equipped with a Kryoflex attachment supplying a nitrogen stream at 150 K. Structure solution and refinement were carried out with SHELXS-97[46] and SHELXL-97[47] using the WinGX[48] software package. Corrections for incident and diffracted beam absorption effects were applied using empirical absorption corrections.[49] All non–hydrogen atoms were refined with anisotropic thermal parameters. The positions of hydrogen atoms of PPh_4^+ counterions and disordered CH_2Cl_2 solvent content were calculated based on stereochemical considerations and refined isotropically. The disordered H_2O content was identified in the D*F* map and refined with isotropic thermal parameters. However, the hydrogen atoms associated with the H_2O content were not possible to be located from the D*F* map and have been omitted from the refinement cycles. Final unit cell data and refinement statistics are collected in Table S1. CCDC numbers 1851991–1851993 contains the supplementary crystallographic data for **1** – **3**. These data can be obtained free of charge from The Cambridge Crystallographic Data Center via www.ccdc.cam.ac.uk/data_request/cif.

EPR Spectroscopy. Continuous wave X-band EPR spectra was recorded on a Bruker ELEXSYS E500 spectrometer. Spectra were simulated using the simulation package XSOPHE.[50] Fluid solution spectra were simulated using a spin Hamiltonian of the form $\hat{H} = g\cdot\mu_B\cdot B\cdot S + a\cdot S\cdot I$, where g is the Landé g-factor, and a is the hyperfine coupling constant for the spin-active ^{122}Pd and ^{195}Pt nuclei in **2** and **3**, respectively; the other parameters have their usual meanings. Satisfactory fits were achieved

using a Lorentzian lineshape with molecular tumbling accommodated by the isotropic liquids model given by $\sigma_v = a + bM_I + cM_I^2$ (Table S4).[51] Randomly orientated EPR spectra were simulated following the spin Hamiltonian $\hat{H} = \mu_B \cdot \mathbf{g} \cdot \mathbf{B} \cdot \mathbf{S} + \sum \mathbf{S} \cdot \mathbf{A} \cdot \mathbf{I}$, where **g** and **A** are the 3 × 3 electron Zeeman and magnetic hyperfine interaction matrices, respectively. A Gaussian lineshape and distribution of *g*- and *A*-values (strain) were employed to account for the linewidth variation (Tables S5).

Pulsed X-band EPR data were measured using a Bruker ELEXSYS E580 spectrometer equipped with an Oxford Instruments CF935 continuous Helium flow cryostat. Samples were prepared by dissolving **1** – **3** in CD_2Cl_2 to a concentration of 1 mM, loading into 3.8 mm o.d. quartz EPR tubes and adding 2% (v/v) DMF-d_7 to aid glassing. The solution samples were degassed via three freeze-pump-thaw cycles, followed by flame sealing. Samples of $[\mathbf{4}]^{2+}$ and $[\mathbf{5}]^{1+}$ were prepared by bulk electrolysis of a 1 mM dichloromethane solution containing 0.2 M $[N(^nBu)_4]PF_6$ as electrolyte. The electrochemical cell was degassed prior to the experiment and the electrolysis conducted under an inert atmosphere. ESE-detected EPR spectra were collected at 10 K (**1** – **3**) and 20 K ($[\mathbf{4}]^{2+}$ and $[\mathbf{5}]^{1+}$) using a Hahn echo pulse sequence ($\pi/2 - \tau - \pi - \tau -$ echo) with a 4-step phase cycle, where $\pi/2$ = 16 ns, π = 32 ns and τ = 400 ns. Simulations were performed as using XSOPHE[50] using the aforementioned spin-Hamiltonian. Phase memory times (T_M) were also measured with a Hahn echo pulse sequence. Decay curves were collected at field positions indicated on ESE spectra. Acquisition times were set to capture the top half of the spin echo and the acquired echo was integrated. The data were phased by maximizing the sum of the data points in the real components of the spectrum and fit to the biexponential function $I(\tau) = y_0 + A_f \exp(-\tau/T_{M,f}) + A_s \exp(-\tau/T_{M,s})$, where f and s indicate fast and slow processes, respectively. Spin-lattice relaxation times (T_1) for **1** – **3** were collect at 10 K following the inversion recovery sequence ($\pi - T - \pi/2 - \tau - \pi - \tau -$ echo) with 4-step phase cycling in which $\pi/2$ = 16 ns, π = 32 ns, and *T* incremented from a starting value of 100 ns. The value of τ was selected to correspond to the maximum in the ESEEM at 400 ns. Acquisition times were set to capture the top half of the spin echo and the acquired echo was integrated. The data were phased by maximizing the sum of the data points in the real components of the spectrum and fit to the biexponential function $I(\tau) = y_0 + A_f \exp(-\tau/T_{1,f}) + A_s \exp(-\tau/T_{1,s})$. Nutation measurements were performed at three different

microwave powers with a nutation pulse of variable length (tipping) pulse followed by a Hahn echo sequence ($t_p - T - \pi/2 - \tau - \pi - \tau -$ echo). Data were collected employing 4-phase cycling, in which in which $\pi/2$ = 16 ns, π = 32 ns and τ = 400 ns for nutation pulse lengths T = 400 ns and 1800 ns. The tipping pulse, t_p, is augmented in 4 ns increments from a starting value of 4 ns. Nutation data was processed by subtracting a stretched exponential baseline from the echo decay, then zero-filling with 1024 or 2048 points, followed by a Fourier transform with a Hamming window.

Other Physical Methods. Cyclic voltammogrammetry measurements were performed with a Metrohm Autolab P128 potentiostat. The electrode configuration consisted of a 2 mm glassy carbon working electrode, a platinum auxiliary electrode and a reference electrode consisting of $Ag/AgNO_3$ (0.01 M in MeCN) incorporated into a salt bridge containing supporting electrolyte (to minimize Ag^+ leakage). Solutions of the complexes (1 – 2 mM) were prepared in dichloromethane containing 0.1 M $[N(^nBu)_4]PF_6$ as electrolyte. All reduction potentials are referenced versus the ferrocenium/ferrocene ($Fc^{+/0}$) couple. Electronic absorption spectra were recorded on a Shimadzu UVA 3600 spectrophotometer (range 200 – 1600 nm). Electrospray ionization (ESI) mass spectra were obtained on a Bruker micrOTOF-Q mass spectrometer.

Calculations. All calculations in this work were performed with the electronic structure program ORCA.[52] Geometry optimizations were carried out using the BP86 functional with dichloromethane as solvent.[53] A segmented all-electron relativistically contracted basis set of triple-ζ-quality (def2-TZVPP) was used for all atoms.[54] A scalar relativistic correction was applied using the zeroth-order regular approximation (ZORA) method[55] as implemented by van Wüllen.[56] In the context of ZORA, a one center approximation has been shown to introduce only minor errors to the final geometries. Auxiliary basis sets for all complexes used to expand the electron density in the calculations were chosen to match the orbital basis. The conductor like screening model (COSMO) was used for all calculations.[57] The self-consistent field calculations were tightly converged (1×10^{-8} E_h in energy, 1×10^{-7} E_h in the density change, and 1×10^{-7} in the maximum element of the DIIS[58] error vector). The geometry search for all complexes was carried out in redundant internal coordinates without

imposing geometry constraints. The property calculations at the optimized geometries were done with the PBE0 hybrid functional[59] and the RIJCOSX algorithm to expedite calculation of the Hartree-Fock exchange.[60] In this case the same basis sets were used but with enhanced integration accuracy (SPECIALGRIDINTACC 10) for the metal and sulfur atoms. Calculation of the **g**-matrix included a larger the integration grid (Grid5) and fully decontracted basis sets.[61]

We used the broken symmetry (BS) approach to describe our computational result of [**4**]$^{2+}$.[62] We adopt the following notation: the given system was divided into two fragments. The notation BS(*m*,*n*) refers then to a broken symmetry state with *m* unpaired α-spin electrons essentially on fragment 1 and *n* unpaired β-spin electrons localized on fragment 2. In most cases, fragments 1 and 2 correspond to the metal and the ligands, respectively. In this notation the standard high-spin, open-shell solution is written as BS(*m* + *n*,0). The BS(*m*,*n*) notation refers to the initial guess to the wave function. The variational process does, however, have the freedom to converge to a solution of the form BS(*m* – *n*,0) in which effectively the *nβ*-spin electrons pair up with *n* < *mα*-spin electrons on the partner fragment. Such a solution is then a standard $M_s \cong (m - n)/2$ spin-unrestricted Kohn-Sham solution. As explained elsewhere,[63] the nature of the solution is investigated from the corresponding orbital transformation (COT) which, from the corresponding orbital overlaps, displays whether the system should be described as a spin-coupled or a closed-shell solution. The exchange coupling constant *J* was calculated on broken-symmetry geometries using Eq. 1,[64] and assuming the spin-Hamiltonian Eq. 2 is valid.

$$J = \frac{E_{HS} - E_{BS}}{\langle \hat{S}^2 \rangle_{HS} - \langle \hat{S}^2 \rangle_{BS}} \quad (1)$$

$$\hat{H} = -2J\hat{S}_A \cdot \hat{S}_B \quad (2)$$

Corresponding[63] and canonical orbitals, and density plots were constructed using the program Molekel.[65]

Acknowledgements

We thank the Royal Society of Chemistry for awarding a J. W. T. Jones Travelling Fellowship Grant (S.S.) and financial support from the University of Glasgow. Support from the National Science Foundation (CHE-0845829 to J.P.D.) is gratefully acknowledged.

Conflict of interest

The authors declare no conflict of interest.

Keywords: ligand radicals · metallodithiolene complexes · EPR spectroscopy · quantum computing · spin-orbit coupling

---

[1] M. N. Leuenberger, D. Loss, *Nature* **2001**, *410*, 789.

[2] S. Sproules, in *Electron Paramagnetic Resonance, Vol. 25* (Eds.: V. Chechik, D. M. Murphy), The Royal Society of Chemistry, Cambridge, UK, **2017**, pp. 61-97.

[3] F. Meier, J. Levy, D. Loss, *Phys. Rev. Lett.* **2003**, *90*, 047901.

[4] F. Meier, J. Levy, D. Loss, *Phys. Rev. B* **2003**, *68*, 134417.

[5] T. D. Ladd, F. Jelezko, R. Laflamme, Y. Nakamura, C. Monroe, J. L. O'Brien, *Nature* **2010**, *464*, 45.

[6] J. M. Zadrozny, J. Niklas, O. G. Poluektov, D. E. Freedman, *ACS Cent. Sci.* **2015**, *1*, 488.

[7] J. Du, X. Rong, N. Zhao, Y. Wang, J. Yang, R. B. Liu, *Nature* **2009**, *461*, 1265.

[8] Y. Dai, Z. Shi, Y. Fu, S. Mu, Y. Wu, J.-H. Su, L. Qin, Y.-Q. Zhai, Y.-F. Deng, X. Rong, J. Du, **2017**, arXiv:1706.09259v09251 [quant-ph].

[9] a) E. Knill, *Nature* **2005**, *434*, 39; b) A. M. Steane, *Nature* **1999**, *399*, 124.

[10] M. J. Graham, C. Yu, M. Krzyaniak, M. R. Wasieleski, D. E. Freedman, *J. Am. Chem. Soc.* **2017**, *139*, 3196.

[11] a) C. Yu, M. J. Graham, J. M. Zadrozny, J. Niklas, M. Krzyaniak, M. R. Wasieleski, O. G. Poluektov, D. E. Freedman, *J. Am. Chem. Soc.* **2016**, *138*, 14678; b) K. Bader, D. Dengler, S. Lenz, B. Endeward, S.-D. Jiang, P. Neugebauer, J. van Slageren, *Nat. Commun.* **2014**, *5*, 5304.

[12] a) M. Atzori, E. Morra, L. Tesi, A. Albino, M. Chiesa, L. Sorace, R. Sessoli, *J. Am. Chem. Soc.* **2016**, *138*, 11234; b) M. Atzori, L. Tesi, S. Benci, A. Lunghi, R. Righini, A. Taschin, R. Torre, L. Sorace, R. Sessoli, *J. Am. Chem. Soc.* **2017**, *139*, 4338; c) K. Bader, M. Winkler, J. van Slageren, *Chem. Commun.* **2016**, *52*, 3623; d) S. Lenz, K. Bader, H. Bamberger, J. van Slageren, *Chem. Commun.* **2017**, *53*, 4477.

[13] a) A. Fernandez, E. Moreno Pineda, C. A. Muryn, S. Sproules, F. Moro, G. A. Timco, E. J. L. McInnes, R. E. P. Winpenny, *Angew. Chem.* **2015**, *127*, 11008; *Angew. Chem. Int. Ed.* **2015**, *54*, 10858; b) J. Ferrando-Soria, S. A. Magee, A. Chiesa, S. Caretta, P. Santini, I. J. Vitorica-Yrezabal, F. Tuna, G. F. S. Whitehead, S. Sproules, K. M. Lancaster, A.-L. Barra, G. A. Timco, E. J. L. McInnes, R. E. P. Winpenny, *Chem* **2016**, *1*, 727; c) J. Ferrando-Soria, E. Moreno Pineda, A. Chiesa, A. Fernandez, S. A. Magee, S. Caretta, P. Santini, I. J. Vitorica-Yrezabal, F. Tuna, G. A. Timco, E. J. L. McInnes, R. E. P. Winpenny, *Nat. Commun.* **2016**, *7*, 11377; d) J. Salinas Uber, M. Estrader, J. Garcia, P. Lloyd-Williams, A. Sadurní, D. Dengler, J. van Slageren, N. F. Chilton, O. Roubeau, S. J. Teat, J. Ribas-Ariño, G. Aromí, *Chem. Eur. J.* **2017**, *23*, 13648.

[14] a) G. A. Timco, S. Carretta, F. Troiani, F. Tuna, R. G. Pritchard, C. A. Muryn, E. J. L. McInnes, A. Ghirri, A. Candini, P. Santini, G. Amoretti, M. Affronte, R. E. P. Winpenny, *Nat. Nanotechnol.* **2009**, *4*, 173; b) A. Ardavan, A. M. Bowen, A. Fernandez, A. J. Fielding, D. Kaminski, F. Moro, C. A. Muryn, M. D. Wise, A. Ruggi, K. Severin, G. A. Timco, C. R. Timmel, F. Tuna, G. F. S. Whitehead, R. E. P. Winpenny, *npj Quantum Inf.* **2015**, *1*, 15012.

[15] D. Aguilà, L. A. Barrios, V. Velasco, O. Roubeau, A. Repollés, P. J. Alonso, J. Sesé, S. J. Teat, F. Luis, G. Aromí, *J. Am. Chem. Soc.* **2014**, *136*, 14215.

[16] S. Nakazawa, S. Nishida, T. Ise, T. Yoshino, N. Mori, R. Rahimi, K. Sato, Y. Morita, K. Toyota, D. Shiomi, M. Kitagawa, H. Hara, P. Carl, P. Höfer, T. Takui, *Angew. Chem.* **2012**, *124*, 9998; *Angew. Chem. Int. Ed.* **2012**, *51*, 9860.

[17] K. Arumugam, M. Selvachandran, A. Obanda, M. C. Shaw, P. Chandrasekaran, S. L. Caston Good, J. T. Mague, S. Sproules, J. P. Donahue, *Inorg. Chem.* **2018**, *57*, 4023.

[18] K. Arumugam, M. C. Shaw, J. T. Mague, E. Bill, S. Sproules, J. P. Donahue, *Inorg. Chem.* **2011**, *50*, 2995.

[19] a) K. Ray, T. Petrenko, K. Wieghardt, F. Neese, *Dalton Trans.* **2007**, 1552; b) S. Sproules, K. Wieghardt, *Coord. Chem. Rev.* **2011**, *255*, 837.

[20] A. Zardadoulas, M. J. Field, C. Papatriantafyllopoulou, J. Fize, V. Artero, C. A. Mitsopoulou, *Inorg. Chem.* **2016**, *55*, 432.

[21] S. Sproules, P. Banerjee, T. Weyhermüller, Y. Yan, J. P. Donahue, K. Wieghardt, *Inorg. Chem.* **2011**, *50*, 7106.

[22] M. J. Graham, M. Krzyaniak, M. R. Wasieleski, D. E. Freedman, *Inorg. Chem.* **2017**, *56*, 8106.

[23] R. Kirmse, E. Möller, C. Seitz, J. Reinhold, *Z. Anorg. Allg. Chem.* **1997**, *627*, 159.

[24] D. D. Sarma, *Proc. Indian Acad. Soc. (Chem. Sci.)* **1981**, *90*, 19.

[25] K. Bader, S. H. Schlindein, D. Gudat, J. van Slageren, *Phys. Chem. Chem. Phys.* **2017**, *19*, 2525.

[26] J. Bendix, M. Brorson, C. E. Schäffer, *Inorg. Chem.* **1993**, *32*, 2838.

[27] J.-L. Du, G. R. Eaton, S. S. Eaton, *Appl. Magn. Reson.* **1994**, *6*, 373.

[28] J. M. Zadrozny, J. Niklas, O. G. Poluektov, D. E. Freedman, *J. Am. Chem. Soc.* **2014**, *136*, 15841.

[29] A. Ardavan, G. A. D. Briggs, *Phil. Trans. R. Soc. A* **2011**, *369*, 3229.

[30] M. Warner, S. Din, I. S. Tupitsyn, G. W. Morley, A. M. Stoneham, J. A. Gardener, Z. Wu, A. J. Fisher, S. Heutz, C. W. M. Kay, G. Aeppli, *Nature* **2013**, *503*, 504.

[31] a) J.-L. Du, G. R. Eaton, S. S. Eaton, *J. Magn. Reson., Ser. A* **1996**, *119*, 240; b) R. Husted, J.-L. Du, G. R. Eaton, S. S. Eaton, *Magn. Reson. Chem.* **1995**, *33*, S66.

[32] a) Y. Kato, R. C. Myers, A. C. Gossard, D. D. Awschalom, *Science* **2003**, *306*, 1910; b) L. Liu, C.-F. Pai, Y. Li, H. W. Tseng, D. C. Ralph, R. A. Burhrman, *Science* **2012**, *336*, 555; c) S. D. Ganichev, E. L. Ivchenko, V. V. Bel'kov, S. A. Tarasenko, M. Sollinger, D. Weiss, W. Wegscheider, W. Prettl, *Nature* **2002**, *417*, 153.

[33] A. Lunghi, F. Totti, R. Sessoli, S. Sanvito, *Nat. Commun.* **2017**, *8*, 14620.

[34] R. Kirmse, J. Stach, W. Dietzsch, G. Steimecke, E. Hoyer, *Inorg. Chem.* **1980**, *19*, 2679.

[35] H. Sato, V. Kathirvelu, A. J. Fielding, J. P. Blinco, A. S. Micallef, S. E. Bottle, S. S. Eaton, G. R. Eaton, *Mol. Phys.* **2007**, *105*, 2137.

[36] a) L. A. Benítez, J. F. Sierra, W. Savero Torres, A. Arrighi, F. Bonell, M. V. Costache, S. O. Valenzuela, *Nat. Phys.* **2018**, *14*, 303; b) W. Yan, O. Txoperena, R. Llopis, H. Dery, L. E. Hueso, F. Casanova, *Nat. Commun.* **2016**, *7*, 13372; c) J. H. Garcia, M. Vila, A. W. Cummings, S. Roche, *Chem. Soc. Rev.* **2018**, *47*, 3359.

[37] S. R. Hartmann, E. L. Hahn, *Phys. Rev.* **1962**, *128*, 2042.

[38] a) K. Arumugam, M. C. Shaw, P. Chandrasekaran, D. Villagrán, T. G. Gray, J. T. Mague, J. P. Donahue, *Inorg. Chem.* **2009**, *48*, 10591; b) K. Arumugam, R. Yu, D. Villagrán, T. G. Gray, J. T. Mague, J. P. Donahue, *Inorg. Chem.* **2008**, *47*, 5570.

[39] M. A. Fox, D. A. Chandler, *Adv. Mater.* **1991**, *3*, 381.

[40] G. R. Eaton, S. S. Eaton, *Acc. Chem. Res.* **1988**, *21*, 107.

[41] P. Lutz, R. Marx, D. Dengler, A. Kromer, J. van Slageren, *Mol. Phys.* **2013**, *111*, 2897.

[42] J. Lehmann, A. Gaita-Ariño, E. Coronado, D. Loss, *Nat. Nanotechnol.* **2007**, *2*, 312.

[43] G. N. Schrauzer, V. P. Mayweg, *J. Am. Chem. Soc.* **1965**, *87*, 1483.

[44] V. D. Makhaev, A. P. Borisov, T. P. Karpova, E. B. Lobkovskii, B. P. Tarasov, A. N. Chekhlov, *Bull. Acad. Sci. USSR., Div. Chem. Sci.* **1989**, *38*, 377.

[45] W. L. F. Armarego, D. D. Perrin, *Purification of Laboratory Chemicals*, 4th ed., Butterworth-Heinemann, Oxford, U.K., **2000**.

[46] G. M. Sheldrick, *Acta Crystallogr. Sect. A* **1990**, *46*, 467.

[47] G. M. Sheldrick, *Acta Crystallogr. Sect. A* **2008**, *64*, 112.

[48] L. J. Farrugia, *J. Appl. Cryst.* **1999**, *32*, 837.

[49] R. C. Clark, J. S. Reid, *Acta Crystallogr. Sect. A* **1995**, *51*, 887.

[50] G. R. Hanson, K. E. Gates, C. J. Noble, M. Griffin, A. Mitchell, S. Benson, *J. Inorg. Biochem.* **2004**, *98*, 903.

[51] a) P. W. Atkins, D. Kivelson, *J. Chem. Phys.* **1966**, *44*, 169; b) R. Wilson, D. Kivelson, *J. Chem. Phys.* **1966**, *44*, 154; c) R. Wilson, D. Kivelson, *J. Chem. Phys.* **1966**, *44*, 4440; d) R. Wilson, D. Kivelson, *J. Chem. Phys.* **1966**, *44*, 4445.

[52] F. Neese, *WIREs Comput. Molec. Sci.* **2012**, *2*, 73-78.

[53] a) A. D. Becke, *J. Chem. Phys.* **1988**, *84*, 4524; b) J. P. Perdew, *Phys. Rev. B* **1986**, *33*, 8822.

[54] D. A. Pantazis, X.-Y. Chen, C. R. Landis, F. Neese, *J. Chem. Theory Comput.* **2008**, *4*, 908.

[55] a) E. van Lenthe, J. G. Snijders, E. J. Baerends, *J. Chem. Phys.* **1996**, *105*, 6505-6516; b) E. van Lenthe, A. van der Avoird, P. E. S. Wormer, *J. Chem. Phys.* **1998**, *108*, 4783-4796; c) J. H. van Lenthe, S. Faas, J. G. Snijders, *Chem. Phys. Lett.* **2000**, *328*, 107-112.

[56] C. J. van Wüllen, *J. Chem. Phys.* **1998**, *109*, 392-399.

[57] A. Klamt, G. Schüürамann, *J. Chem. Soc., Perkin Trans. 2* **1993**, 799.

[58] a) P. Pulay, *Chem. Phys. Lett.* **1980**, *73*, 393; b) P. Pulay, *J. Comput. Chem.* **1982**, *3*, 556.

[59] a) J. P. Perdew, K. Burke, M. Ernzerhof, *Phys. Rev. Lett.* **1996**, *77*, 3865; b) C. Adamo, V. Barone, *J. Chem. Phys.* **1999**, *110*, 6158.

[60] a) F. Neese, F. Wennmohs, A. Hansen, U. Becker, *Chem. Phys.* **2009**, *356*, 98-109; b) R. Izsák, F. Neese, *J. Chem. Phys.* **2011**, *135*, 144105.

[61] a) F. Neese, *J. Chem. Phys.* **2001**, *115*, 11080; b) F. Neese, *J. Chem. Phys.* **2003**, *118*, 3939.

[62] a) L. Noodleman, *J. Chem. Phys.* **1981**, *74*, 5737-5743; b) L. Noodleman, D. A. Case, A. Aizman, *J. Am. Chem. Soc.* **1988**, *110*, 1001-1005; c) L. Noodleman, E. R. Davidson, *Chem. Phys.* **1986**, *109*, 131-143; d) L. Noodleman, J. G. Norman, J. H. Osborne, A. Aizman, D. A. Case, *J. Am. Chem. Soc.* **1985**, *107*, 3418-3426; e) L. Noodleman, C. Y. Peng, D. A. Case, J. M. Monesca, *Coord. Chem. Rev.* **1995**, *144*, 199-244.

[63] F. Neese, *J. Phys. Chem. Solids* **2004**, *65*, 781-785.

[64] a) T. Soda, Y. Kitagawa, T. Onishi, Y. Takano, Y. Shigetu, H. Nagao, Y. Yoshioka, K. Yamaguchi, *Chem. Phys. Lett.* **2000**, *319*, 223; b) K. Yamaguchi, Y. Takahara, T. Fueno, in *Applied Quantum Chemistry* (Ed.: V. H. Smith), Reidel, Dordrecht, The Netherlands, **1986**, p. p. 155.

[65] *Molekel*, Advanced Interactive 3D-Graphics for Molecular Sciences, Swiss National Supercomputing Center. https://ugovaretto.github.io/molekel/